Largest aftershock nucleation driven by afterslip during the 2014 Iquique sequence

Yuji Itoh[1*], Anne Socquet[1] and Mathilde Radiguet[1]

[1]Univ. Grenoble Alpes, Univ. Savoie Mont Blanc, CNRS, IRD, Univ. Gustave Eiffel, ISTerre, 38000 Grenoble, France

*Corresponding author: Yuji Itoh (yuji.itoh@univ-grenoble-alpes.fr)

Abstract

Various earthquake source models predict that aseismic slip modulates the seismic rupture process. However, observations of aseismic slip associated with earthquakes are scarce, which has left the earthquake source model controversial. Here, we characterise seismic and aseismic processes for 3 days during the 2014 Iquique earthquake sequence in northern Chile by analysing seismicity and crustal deformation time series measured by high-rate Global Positioning System (GPS). We demonstrate that the early afterslip started immediately after the M 8.1 mainshock and led to the largest M 7.6 aftershock 27 hours later, located ~120 km to the south. At the mainshock latitude, the interevent early afterslip is located downdip of the mainshock rupture, and is associated with aftershocks. These afterslip and aftershocks exhibit a rapid temporal decay. In contrast, south of the mainshock slip patch, a peak of afterslip separates the mainshock rupture from the largest aftershock, suggesting that this area acted as a barrier to the southward propagation of the mainshock rupture. Seismicity count and moment accelerate in this southern area during the interevent stage. We conclude that the largest aftershock nucleation was driven by the interevent afterslip. The mechanical connection between sequential great earthquakes can therefore be mediated by aseismic slip.

Main text

Subduction zone megathrust faults host diverse slip behaviours. Seismic (fast with large shaking) and aseismic (slow with little or no shaking) slip are two complementary classes[1] that interact with each other. Mechanical models of the earthquake source process have been developed by laboratory experiments and analytical or numerical simulations[2-6]. These models show that seismic-aseismic interaction is commonly involved in nucleation, propagation and termination of seismic ruptures, as well as during the post-seismic phase which involves both afterslip and aftershocks. Observational evidence of nucleation is, however, limited to a small number of well-monitored large earthquakes due to their subtle signals and/or short duration[7-20]. Although seismic processes are resolved at time scales down to seconds, subdaily dynamics of aseismic processes are poorly documented, because GPS coordinates used for its investigation are usually limited to a daily sampling interval. Observation of aseismic processes with higher temporal resolution is required to unravel the dynamics of seismic-aseismic interaction, notably during nucleation.

Large earthquakes are followed by aftershocks[21] that relax stress change induced by the mainshock. The largest aftershock follows the mainshock with a spatial offset and time delay that can vary greatly from one case to the other[16,22-27]. However, the mechanism for this delay is not well understood. The propagation of seismic ruptures are often arrested at adjacent patches, prone to slow slip[28-30]. Spatiotemporal aftershock evolution is often modulated by background aseismic slip[31]. Therefore, seismic-aseismic interaction could provide a causal link in the delayed occurrence of the largest aftershock. Nevertheless, direct observational evidence of the interaction processes is lacking. The 2014 M 8.1 Iquique earthquake in northern Chile along the Nazca megathrust is known as one of the events preceded by vigorous precursory seismic and aseismic activities[16-20]. Its largest aftershock (M 7.6, Fig. 1a)[17,22-25] occurred only ~120 km south of, and ~27 hours following the mainshock. Interevent processes between the two events have so far remained elusive, because the very short duration is challenging with the daily GPS data. This study investigates source processes during the 2014 Iquique sequence and their implications for earthquake mechanics by unveiling the interevent aseismic processes using high-rate GPS and comparing them with seismicity.

Discovery of aseismic deformation and slip during the 2014 Iquique sequence

We identified transient crustal deformation during the 27 hour period between the 2014 Iquique mainshock and the largest aftershock by analysing high-rate GPS coordinates at an interval of 5 minutes (Figs. 1c-e). After removing spatiotemporally correlated noise (Extended Data Fig. 1; See Methods), a slow transient motion between the mainshock and its largest aftershock is clearly visible (Figs. 1c-e and Extended Data Figs. 2a-c). Following the largest aftershock, a similar transient motion emerged again, but a larger amplitude is observed near the aftershock's epicentre (Figs. 1c-e). We fitted a trajectory model consisting of step and logarithmic functions to the cleaned time series and obtained displacements during four stages, namely, the interevent, the post-largest-aftershock, and the two coseismic stages, from the model prediction (See Methods). This approach allowed us to robustly extract cumulative displacements (Fig. 1b and Extended Data Figs. 2d and 3a-f). Interevent displacements point towards the source area at most GPS sites (Fig. 1b), indicating a trenchward postseismic deformation pattern typical for offshore megathrust events[32-33]. These surface observations are compatible with the occurrence of afterslip. Two-day postseismic displacements following the largest aftershock similarly indicate trenchward motion but with a different spatial pattern; the largest displacement is observed near the epicentre of the largest aftershock, indicating that it additionally excited afterslip (Extended Data Fig. 3c). We imaged the slip distribution along the megathrust by inverting the extracted surface displacements associated with the aseismic slip and both earthquakes (See Methods, Fig. 2 and Extended Data Figs. 2e and 3g-h). This allows us to depict the interplay of seismic and aseismic slip in a methodologically consistent manner, although many other models were already published[17,20,22-25].

Interplay of seismic and aseismic slip and implications for megathrust segmentation

The imaged interevent cumulative afterslip has two peaks (blue contours in Fig. 2a and Extended Data Fig. 2e). The largest afterslip peak is located down-dip of the mainshock slip (Fig. 2a), a typical afterslip feature due to the depth-dependent change in megathrust rheology[1]. Moderate seismicity (aftershocks) down-dip of the mainshock slip[34] is located next to this afterslip peak. Moderate seismicity up-dip of the mainshock slip may contain repeating earthquakes[24], implying another peak of afterslip, which is, however, not resolvable with land GPS observations alone. The other resolved afterslip peak is located south of the mainshock slip peak, at a seismogenic depth with moderate seismicity. This peak of slip is not an artefact of the inversion, but is supported by the displacements recorded at coastal sites at ~20.2°S (Extended Data Fig. 4). The two-day afterslip following the largest aftershock is also located close to these two peaks with different amplitudes; the slip is larger in the southern region close to the largest aftershock (green contours in Fig. 2 and Extended Data Fig. 3i). The afterslip distribution over a longer 9-month period[33] contains these two afterslip areas, indicating that they represent an aseismic megathrust.

The inferred interevent afterslip located between the two epicentres explains the spatial separation of the mainshock and its largest aftershock (Fig. 2). Fault zones prone to hosting aseismic creep are usually not involved in the dynamic seismic rupture[28-30]. Hence, this interevent afterslip area likely acted as an aseismic barrier to the southward propagation of the mainshock rupture[22-25] (Fig. 3b), and delayed the rupture of the seismic asperity associated with the largest aftershock, despite a positive mainshock Coulomb Stress Change (CSC)[21] at the largest aftershock epicentre (Extended Data Fig. 5a). This aseismic barrier was proposed by a previous study of afterslip for 9 months following the largest aftershock[33]. The occurrence of interevent afterslip in this same area unambiguously confirms the barrier behaviour. We speculate that such aseismic barrier behaviour at seismogenic depths is hosted by irregular megathrust geometry[35] inferred offshore of Iquique from gravity anomaly data[36-37], subparallel faults along the megathrust[38] and seamounts at depth[39] (Fig. 1a and Extended Data Fig. 6).

The megathrust offshore of Iquique has shown creeping behaviour at different stages of the seismic cycle (Fig. 3a). Different long-term interseismic locking models tend to show lower degrees of locking to the south and north of the mainshock section (Fig. 3b)[40-42]. The pre-mainshock aseismic transient over 8 months (black contours in Figs. 3a-b)[18] overlaps with these aseismic slip regions. Therefore, one possible interpretation is that these regions represent persistent aseismic barriers to adjacent megathrust ruptures[28-30] (Fig. 3b) as a zone of velocity-strengthening friction[6]. However, in the southern offshore Iquique area at ~20.5°S, the along-strike location of the inferred aseismic barrier does not coincide with the segmentation boundary of the 1868 M_w 8.8 South Peru and the 1877 M_w 8.5 Northern Chile earthquakes, although it is in the 1877 rupture area (Figs. 1a and 4b and Extended Data Fig. 6)[43-44]. As it was partly involved with the largest aftershock rupture (Fig. 2), it is not a permanent barrier, and can therefore be broken during larger earthquakes[5]. In contrast, we speculate that the northern area is a persistent aseismic barrier because it coincides with the possible end of the 1877 rupture (Fig. 1a), as well as excess fluid pressure along the megathrust[45]. There is another afterslip peak overlapping with the 8-month pre-mainshock slip peak at greater depth (Fig. 3a), which implies the persistent aseismic behaviour controlled by a ductile fault rheology[1].

Afterslip drove the largest aftershock nucleation

The temporal evolution of the interevent seismicity, deformation and slip can provide further details on the interplay between seismic and aseismic slip that led to the largest aftershock. We investigate the interevent site motion by calculating the moving median of the cleaned GPS time series (window length = 0.5 days) (Fig. 4b; See Methods). This approach keeps more information from the original observations than the trajectory model fits for which time constants are poorly constrained (Extended Data Fig. 7). Motograms of the smoothed time series display coherent trenchward motion in front of the interevent afterslip area, concordant at the first order with the trajectory model fit (Figs. 1b and 4a). Coastal sites near Iquique, in front of the southern interevent afterslip area, show a southward deflection of the motion during the late interevent stage, starting ~15 hours after the mainshock (Fig. 4a). This temporal change in displacement pattern is more clearly illustrated by a separate analysis of the first and second halves of the interevent stage. The motion of sites near the mainshock decay more rapidly than sites at the largest aftershock latitude (Figs. 4e-f), which can be interpreted as reflecting a temporal change in the slip pattern.

We inverted the GPS displacements during these two time windows to image the temporal evolution of the interevent slip, which should be mostly aseismic with some seismic contribution from moderate seismicity, including the M 6.1 event which occurs ~45 minutes before the largest aftershock[46] (Figs. 4e-f; See Methods). We spatially divided the studied area north and south of 20.2°S to highlight the first-order contrast in the temporal processes in the mainshock and the largest aftershock areas. We calculated the geodetic moment of the two stages in each area and normalised them by the cumulative value to better illustrate the difference in the temporal process (Fig. 4d).
For seismicity, we employed a machine-learning-based catalogue which lists many moderate aftershocks[34] (Figs. 2a and 4e-g) among available catalogues[34,46-47]. We calculated the cumulative seismicity count and moment in the two areas and normalised them, as was done for the geodetic moment (Figs. 4c-d; See Methods).
In the northern area, where the afterslip is located in the down-dip extension of the mainshock, the interevent slip and its geodetic moment decay quickly (Figs. 4e-f); the moment release ratio between the second and the first stages (hereafter, RM) is only 24%. The moment evolution inferred from seismicity also shows a similar tendency (RM = 9%, see Fig. 4d), despite the gentler decay of seismicity counts during the second stage than the geodetic moment (Fig. 4c), because most of the larger events occurred during the first stage (Fig. 4g). The locations of the peak slip and of the seismicity do not coincide, but the moderate aftershocks and afterslip probably coevolve here.
In contrast, in the southern area, the geodetic slip and the seismicity exhibit quite different temporal evolution histories (Figs. 4c-d). The geodetic slip decays over time with a slower moment decay than in the northern area (Figs. 4d-f; RM = 38%) while the seismicity rate increases with time, together with a great increase of intermittent moment release, dominated by the M 6.1 event that occurs at the extreme end of the interevent stage. (Figs. 4c-g; RM >= 500%). These seismicity events do not exhibit clear southward migration, although aftershock migration is typically found following great earthquakes and is possibly driven by afterslip[26,31]. The M 6.1 event occurred close to the largest aftershock epicentre (~32 km), which might be an indication of a cascade-up process during the largest aftershock nucleation phase driven only by stress change of each event in the pre-event sequence[48]. However, the evidence of continuous geodetic slip does not favour this interpretation. The nucleation process of the Iquique largest aftershock seems rather to be a mixture of seismic and aseismic processes. This scenario favours the rate-dependent cascade-up model which proposes that either concurrent precursor aseismic slip and associated seismicity can ignite the mainshock dynamic rupture[2]. Rough fault geometry can be responsible for such seismic-aseismic mixture during the nucleation process[3-4], consistent with the irregular megathrust structure offshore of Iquique[36-39] (Fig. 1a and Extended Data Fig. 6). We interpret the negative CSC, due to the interevent slip in the largest aftershock epicentral area, as a cumulative stress drop of the aseismic driver (Extended Data Fig. 5b). However, the cascading seismicity, especially the M 6.1 event, probably loaded the largest aftershock epicentre instantaneously during the interevent stage.

Discussion and Conclusions

By analysing the 5-min GPS coordinates, we discovered that the aseismic portion of the megathrust separated, both in space and time, the 2014 Iquique mainshock from its largest aftershock. Similarly, other megathrust earthquakes in Japan and Chile are known to have involved spatiotemporally close large earthquake sequences and interevent afterslip[26-27]. These examples, coupled with our findings, indicate that the local mosaic of seismic and aseismic slip patches must play an important role in controlling the sequential activity of large megathrust earthquakes.

Furthermore, we found, by investigating the temporal history of interevent seismic and aseismic processes, that the largest aftershock nucleation was driven by the mainshock-induced afterslip. The interplay of precursory seismic and aseismic processes has been reported for some events including the 2011 M_w 9.0 Tohoku-oki earthquake and the Iquique mainshock[7-20]. Some of these aseismic precursors represent spontaneous slow slip with[8,10-12,15,19] or without[13-14] acceleration, while some represent decaying afterslip of the main foreshock[7] (including our result). Hence, the large earthquake nucleation phase does not necessarily involve accelerating aseismic slip[3,14]; aseismic slip in any mode can introduce fault instability toward the subsequent event occurrence. Careful re-examination of GPS data utilising high-rate processing would probably yield additional examples of large earthquake nucleation processes triggered by aseismic slip at the hourly scale, and would contribute significantly to our improved understanding of fault slip dynamics.

References

1. Scholz, C. Earthquakes and friction laws. *Nature* **391**, 37–42 (1998).
2. McLaskey, G. C. Earthquake Initiation From Laboratory Observations and Implications for Foreshocks. *J. Geophys. Res.* **124**, 12882– 12904 (2019).
3. Cattania, C. & Segall, P. Precursory slow slip and foreshocks on rough faults. *J. Geophys. Res.* **126**, e2020JB020430 (2021).
4. Romanet, P., Bhat, H. S., Jolivet, R. et al. Fast and slow slip events emerge due to fault geometrical complexity. *Geophys. Res. Lett.* **45**, 4809– 4819 (2018).
5. Kaneko, Y., Avouac, J. P. & Lapusta, N. Towards inferring earthquake patterns from geodetic observations of interseismic coupling. *Nat. Geosci.* **3**, 363–369 (2010).
6. Perfettini, H. & Avouac, J.-P. Postseismic relaxation driven by brittle creep: A possible mechanism to reconcile geodetic measurements and the decay rate of aftershocks, application to the Chi-Chi earthquake, Taiwan, *J. Geophys. Res.* **109**, B02304 (2004).
7. Ohta, Y., Hino, R., Inazu, D. et al. Geodetic constraints on afterslip characteristics following the March 9, 2011, Sanriku-oki earthquake, Japan. *Geophys. Res. Lett.* **39**, L16304 (2012).
8. Caballero, E., Chounet, A., Duputel, Z et al. Seismic and aseismic fault slip during the initiation phase of the 2017 $M_W = 6.9$ Valparaíso earthquake. *Geophys. Res. Lett.*, **48**, e2020GL091916 (2021).
9. Ito, Y., Hino, R., Kido, M. et al. Episodic slow slip events in the Japan subduction zone before the 2011 Tohoku-Oki earthquake. *Tectonophys*. **600**, 14-26 (2013).
10. Kato, A., Obara K., Igarashi T. et al. Propagation of Slow Slip Leading Up to the 2011 $\mathrm{M_w}$ 9.0 Tohoku-Oki Earthquake. *Science* **335**, 705-708 (2012).
11. Marill, L., Marsan, D., Socquet, A. et al. Fourteen-year acceleration along the Japan Trench. *J. Geophys. Res.* **126**, e2020JB021226. (2021).
12. Mavrommatis, A. P., Segall, P., & Johnson, K. M. A decadal-scale deformation transient prior to the 2011 M_w 9.0 Tohoku-oki earthquake, *Geophys. Res. Lett.*, **41**, 4486–4494 (2014).
13. Radiguet, M., Perfettini, H., Cotte, N. et al. Triggering of the 2014 $M_\mathbf{w}$7.3 Papanoa earthquake by a slow slip event in Guerrero, Mexico. *Nature Geosci.* **9**, 829–833 (2016).
14. Voss N., Dixon T. H., Liu Z. et al. Do slow slip events trigger large and great megathrust earthquakes? *Sci Adv* **4**, eaat8472 (2018).
15. Kato, A., Fukuda, J., Kumazawa, T. et al. Accelerated nucleation of the 2014 Iquique, Chile Mw 8.2 Earthquake. *Sci Rep* **6**, 24792 (2016).
16. Schurr, B., Asch, G., Hainzl, S. et al. Gradual unlocking of plate boundary controlled initiation of the 2014 Iquique earthquake. *Nature* **512**, 299–302 (2014).
17. Ruiz, S., Metois, M., Fuenzalida, A. et al. Intense foreshocks and a slow slip event preceded the 2014 Iquique Mw 8.1 earthquake. *Science* **345**, 1165-1169 (2014)
18. Socquet, A., Valdes, J. P., Jara, J. et al. An 8 month slow slip event triggers progressive nucleation of the 2014 Chile megathrust, *Geophys. Res. Lett.* **44**, 4046–4053 (2017).
19. Twardzik, C., Duputel, Z., Jolivet, R. et al. Bayesian inference on the initiation phase of the 2014 Iquique, Chile, earthquake. *Earth Planet. Sci. Lett.* **600**, 117835 (2022).
20. Boudin F., Bernard, P., Meneses, G. et al. Slow slip events precursory to the 2014 Iquique Earthquake, revisited with long-base tilt and GPS records, *Geophys. J. Int.* **228**, 2092–2121 (2022).
21. King, G. C. P., Stein, S. S. & Lin, J. Static stress changes and the triggering of earthquakes. *Bullet. Seismol. Soc. Am.* **84**, 935–953 (1994).
22. Duputel, Z., Jiang, J., Jolivet, R. et al. The Iquique earthquake sequence of April 2014: Bayesian modelling accounting for prediction uncertainty, *Geophys. Res. Lett.* **42**, 7949– 7957 (2015).
23. Jara, J., Sánchez-Reyes, H., Socquet, A. et al. Kinematic study of Iquique 2014 Mw 8.1 earthquake: Understanding the segmentation of the seismogenic zone. *Earth Planet. Sci. Lett.* **503**, 131-143 (2018).

24. Meng, L., Huang, H., Bürgmann, R. et al. Dual megathrust slip behaviors of the 2014 Iquique earthquake sequence. *Earth Planet. Sci. Lett.* **411**, 177-187. (2015).
25. Hayes, G., Herman, M., Barnhart, W. et al. Continuing megathrust earthquake potential in Chile after the 2014 Iquique earthquake. *Nature* **512**, 295–298 (2014).
26. Klein, E., Potin, B., Pasten-Araya, F. et al. Interplay of seismic and a-seismic deformation during the 2020 sequence of Atacama, Chile. *Earth Planet. Sci. Lett.* **570**, 117081 (2021).
27. Miyazaki, S., & Larson, K. M. Coseismic and early postseismic slip for the 2003 Tokachi-oki earthquake sequence inferred from GPS data. *Geophys. Res. Lett.* **35**, L04302 (2008).
28. Perfettini, H., Avouac, JP., Tavera, H. et al. Seismic and aseismic slip on the Central Peru megathrust. *Nature* **465**, 78–81 (2010).
29. Rolandone, F., Nocquet, J.-M., Mothes, P. A. et al. Areas prone to slow slip events impede earthquake rupture propagation and promote afterslip. *Sci. Adv.* **4**, eaao6596 (2018).
30. Nishikawa, T., Matsuzawa, T., Ohta, K. et al. The slow earthquake spectrum in the Japan Trench illuminated by the S-net seafloor observatories. *Science* **365**, 808-813 (2019).
31. Perfettini, H., Frank, W. B., Marsan, D. et al. A model of aftershock migration driven by afterslip. *Geophys. Res. Lett*. **45**, 2283– 2293 (2018).
32. Hoffmann, F., Metzger, S., Moreno, M. et al. Characterizing afterslip and ground displacement rate increase following the 2014 Iquique-Pisagua M_w 8.1 earthquake, Northern Chile. *J. Geophys. Res.*, **123**, 4171–4192 (2018).
33. Shrivastava, M.N., González, G., Moreno, M. et al. Earthquake segmentation in northern Chile correlates with curved plate geometry. *Sci. Rep.* **9**, 4403 (2019).
34. McBrearty, I. W., Gomberg, J., Delorey A. A. et al. Earthquake Arrival Association with Backprojection and Graph Theory. *Bull. Seismol. Soc. Am.* **109**, 2510–2531 (2019).
35. Wang, K. & Bilek S. L. Do subducting seamounts generate or stop large earthquakes? *Geology* **39**, 819–822 (2011).
36. Molina, D., Tassara, A., Abarca, R et al. Frictional segmentation of the Chilean megathrust from a multivariate analysis of geophysical, geological, and geodetic data. *J. Geophys. Res.*, **126**, e2020JB020647 (2021)
37. Maksymowicz, A., Ruiz, J., Vera Emilio., et al. Heterogeneous structure of the Northern Chile marine forearc and its implications for megathrust earthquakes. *Geophys. J. Int.* **215**, 1080–1097 (2018).
38. Cubas, N., Agard, P. & Tissandier, R. Earthquake ruptures and topography of the Chilean margin controlled by plate interface deformation. *Solid Earth* **13**, 779–792 (2022).
39. Geersen, J., Ranero, C., Barckhausen, U. et al. Subducting seamounts control interplate coupling and seismic rupture in the 2014 Iquique earthquake area. *Nat. Commun.* **6**, 8267 (2015).
40. Métois, M., Vigny, C. & Socquet, A. Interseismic Coupling, Megathrust Earthquakes and Seismic Swarms Along the Chilean Subduction Zone (38°–18°S). *Pure Appl. Geophys.* **173**, 1431–1449 (2016).
41. Jolivet, R., Simons, M., Duputel, Z. et al. Interseismic loading of subduction megathrust drives long-term uplift in Northern Chile. *Geophys. Res. Lett.* **47**, e2019GL085377 (2020).
42. Li, S., Moreno, M., Bedford, J. et al. Revisiting viscoelastic effects on interseismic deformation and locking degree: A case study of the Peru-North Chile subduction zone. *J. Geophys. Res.* **120**, 4522–4538 (2015).
43. Comte, D. & Pardo, M. Reappraisal of great historical earthquakes in the northern Chile and southern Peru seismic gaps. *Nat. Hazards*, **4**, 23–44 (1991).
44. Kausel, E. Los terremotos de agosto de 1868 y mayo de 1877 que afectaron el sur del Perú y norte de Chile. *Boletín de la Academia Chilena de Ciencias* **3**, 8–13 (1986).
45. Ma, B., Geersen, J., Lange, D. et al. Megathrust reflectivity reveals the updip limit of the 2014 Iquique earthquake rupture. *Nat. Commun.* **13**, 3969 (2022).

46. Soto, H., Sippl, C., Schurr, B. et al. Probing the northern Chile megathrust with seismicity: the 2014 M8.1 iquique earthquake sequence. *J. Geophys. Res.* **124**, 12935– 12954 (2019)
47. Sippl, C., Schurr, B., Asch, G. et al. Seismicity structure of the northern Chile forearc from >100,000 double-difference relocated hypocenters. *J. Geophys. Res.*, **123**, 4063– 4087 (2018).
48. Ellsworth, W.L. & Bulut, F. Nucleation of the 1999 Izmit earthquake by a triggered cascade of foreshocks. *Nature Geosci.* **11**, 531–535 (2018).
49. DeMets, C., Gordon, R. G. & Argus, D. F. Geologically current plate motions. *Geophys. J. Int.* **181**, 1–80 (2010).
50. Hayes, G. Slab2 - A comprehensive subduction zone geometry model. *U.S. Geological Survey data release* (2018).

Figures

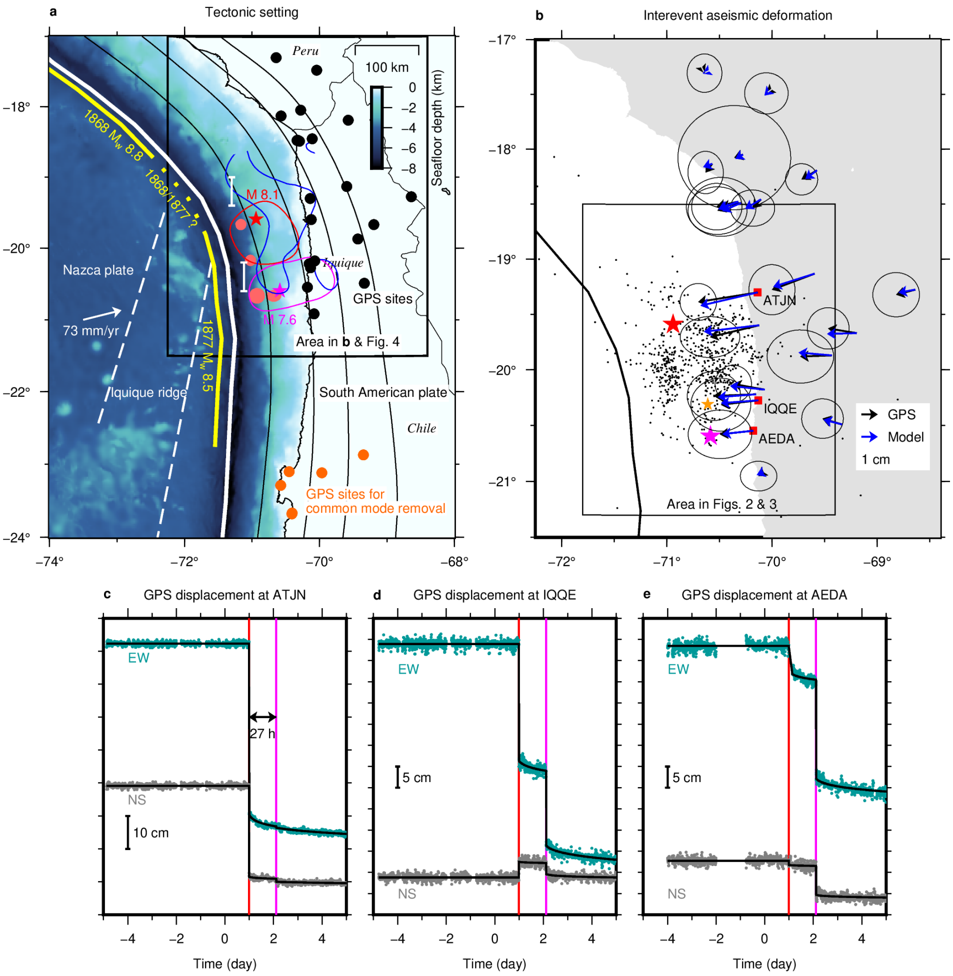

Figure 1. Tectonic setting of Northern Chile and GPS deformation associated with the 2014 Iquique sequence. **a**, Black and orange dots indicate GPS sites for co- and post-seismic deformation analysis and common mode noise extraction, respectively (See Methods for details). Red and purple stars indicate the epicentres of the 2014 Iquique mainshock and the largest aftershock, respectively[46]. Red, blue and purple curves outline slip areas of the mainshock, interevent afterslip and the largest aftershock derived in this study. A white vector offshore indicates Nazca plate motion with respect to the South American plate with its rate labelled[49]. Black contours indicate slab interface depth (20 km interval starting from 20-km depth)[50]. The plate boundary is outlined with a white solid curve. Yellow lines offshore indicate rupture extension of the 1868 and 1877 earthquakes with a controversial section shown as a dotted line[43-44]. Red ovals indicate seamounts at depth[39]. Latitudinal range of inferred aseismic barriers is shown with two white bars offshore. **b**, Horizontal GPS displacements (black vectors) during 27 hours between the mainshock and the largest aftershock, together with the model prediction (blue vectors) from aseismic slip inversion shown in Fig. 2**a** and Extended Data Fig. 2**e**. Red squares indicate GPS site locations, time series of which are shown in **c** – **e**. Black dots indicate seismicity in the same time window[34]. **c** – **e**, Cleaned 5-minute high-rate GPS horizontal coordinates at selected sites as labelled. Overlying black lines are trajectory model fits. Red and pink vertical lines indicate the timings of the mainshock and the largest aftershock, respectively[46], and a two-headed arrow indicates the interevent stage of our main interest. Site location is shown in **b** as red squares.

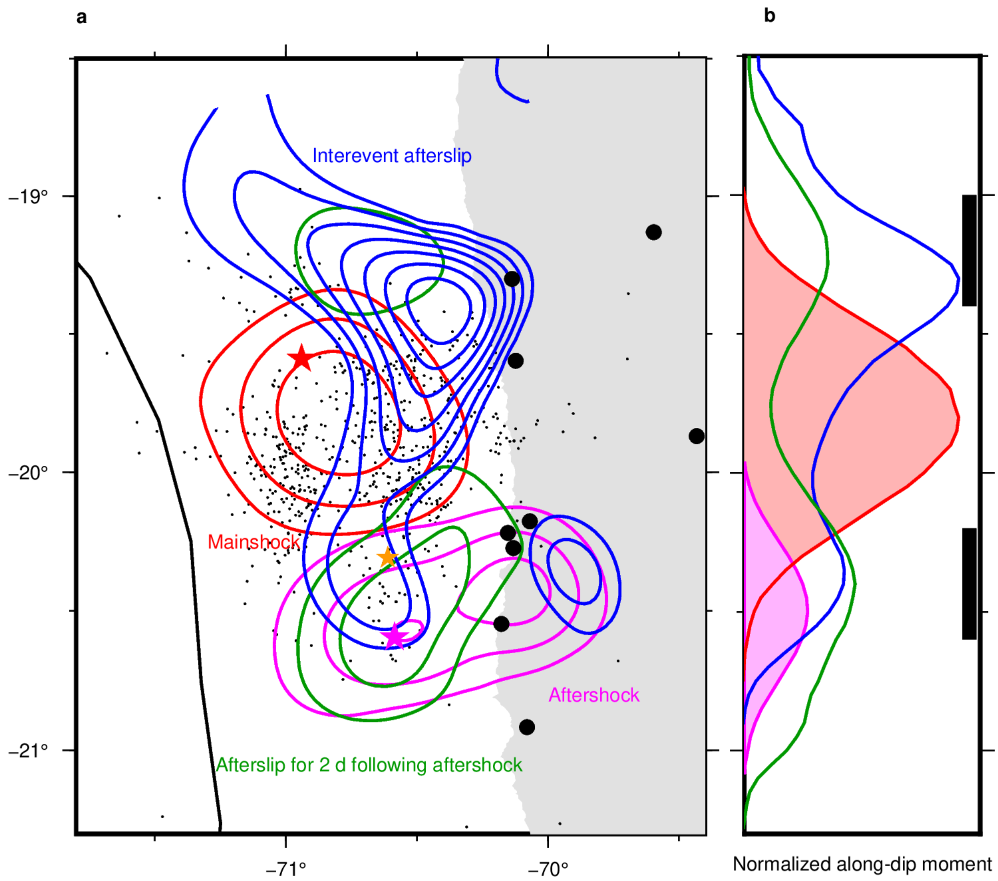

Figure 2. a, Comparison of the mainshock coseismic slip (1 m interval starting from 2 m), cumulative interevent afterslip (4 cm interval starting from 8 cm), the largest aftershock coseismic slip (20 cm interval starting from 40 cm) and afterslip following the largest aftershock (4 cm interval starting from 8 cm) as labelled. All the slip models are derived from displacements obtained through the trajectory model fitting (Figs. 1**c**-**e**, Extended Data Fig. 2**a**-**c**; See Methods). Black dots indicate seismicity during the interevent stage[34]. Black dots GPS indicate site location. **b**, Normalised along-dip moment with respect to latitude. Seismic (red and purple) and aseismic (blue and green) moments are separately normalised with respect to their maximum values. The aseismic-to-seismic ratio of the normalising factors is ~0.056. Each colour corresponds to that used in **a**. Two black bars indicate the inferred aseismic barrier location.

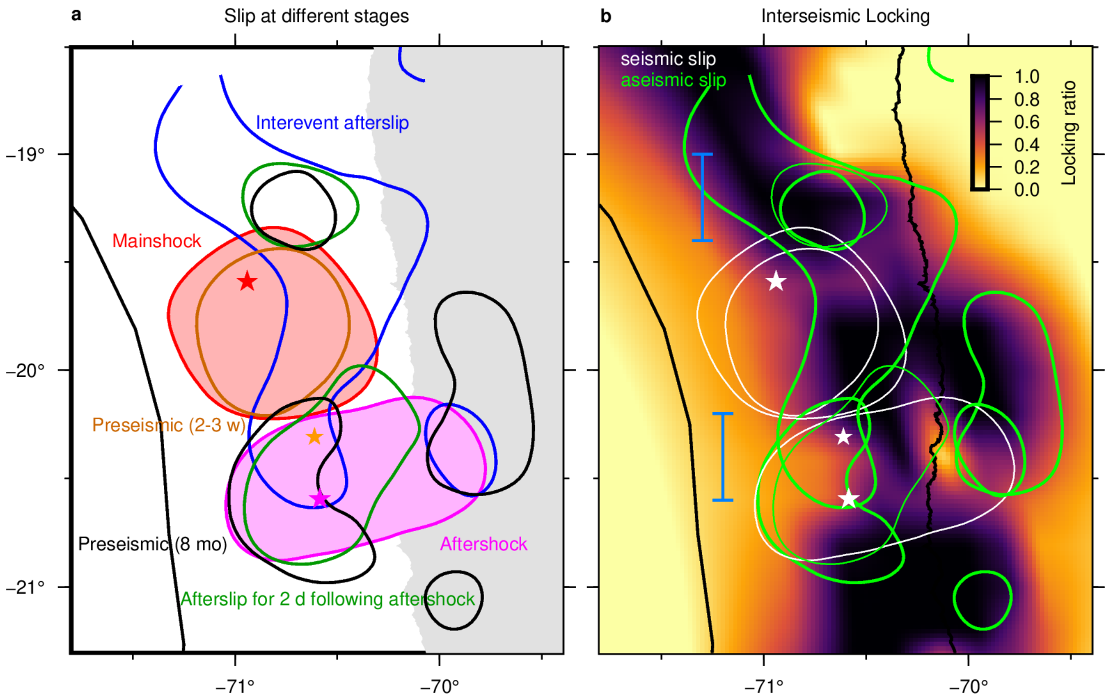

Figure 3. **a**, Compilation of seismic and aseismic slip events in the region at different stages as labelled. These contours outline areas which experienced slip of more than 2 m (mainshock; red), 8 cm (interevent afterslip; blue), 40 cm (largest aftershock; purple), 8 cm (afterslip for 2 days following largest aftershock; green), 5 mm (pre-mainshock for 8 months; black)[18] and 5 cm (pre-mainshock for 2-3 weeks; brown)[18]. **b**, Slip events at different stages (event information shown in **a**) with interseismic locking (background colour)[40]. Seismic and aseismic slip events are drawn with white and green contours, respectively, for clarity. We regard the preseismic (2 – 3 weeks) slip as seismic slip because ~65% of moment release was released seismically[18]. Latitudinal range of inferred aseismic barriers is shown with two light blue bars offshore.

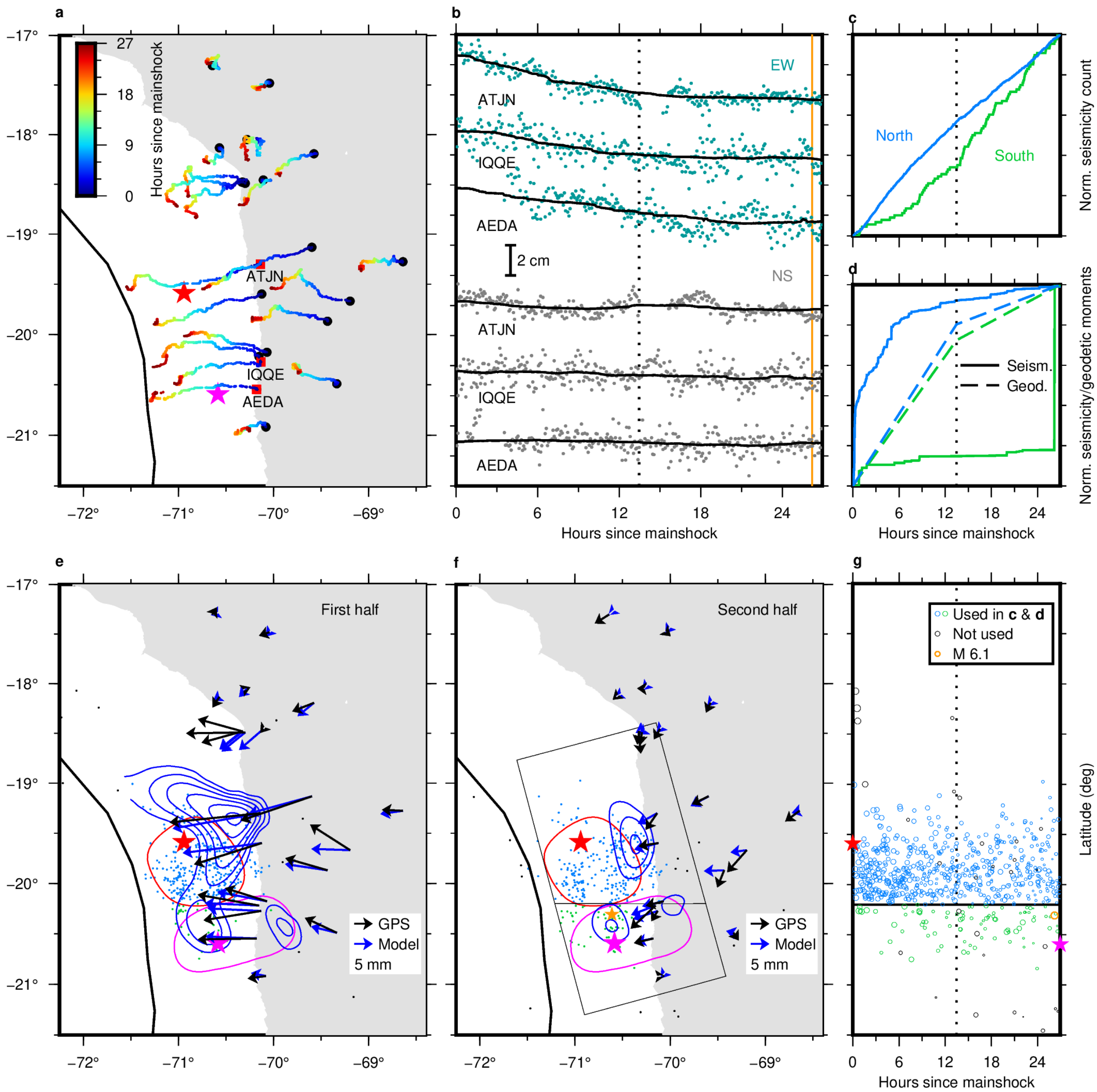

Figure 4. **a**, Trajectory of three GPS sites during 27 hours between the mainshock and the largest aftershock colour-coded with time. **b**, Interevent GPS coordinates (dots) and their moving median (0.5-day window; solid lines). Site and components are labelled. The location of these sites is shown in **a**. A dotted vertical line shows a middle point of the interevent stage. **c**, Normalised seismicity count in the two regions divided at 20.2°S as labelled. Events accounted for in the calculation[34] are shown in **e** – **f** with corresponding colours. **d**, Same as **c** but with normalised seismicity moment (solid lines). The broken lines indicate the evolution of geodetic moment by assuming a linear evolution during the two stages. **e** – **f**, Interevent afterslip snapshots (contours; 4 cm interval starting from 4 cm) inferred by inverting displacements during the first (**e**) and the second (**f**) halves of the interevent stage which are derived from the moving median analysis (black vectors; **b**). Error ellipses of GPS are not shown for clarity. GPS displacements at sites north of 19°S are not inverted. Slip areas of the mainshock and the largest aftershock are outlined with red and purple curves with their epicentres[46] using the same colours. The orange star indicates the M 6.1 earthquake ~45 minutes before the largest aftershock[46]. **g**, Seismicity between the mainshock and the largest aftershock (open circles scaled with magnitude)[34].

Methods

GPS data cleaning

We removed spatiotemporally correlated fluctuations in 5-minute high-rate GPS coordinates processed by Nevada Geodetic Laboratory[51] through the following procedure. First, we fixed the GPS coordinates into the South American plate using a plate motion model with respect to ITRF2014[52] (black in Extended Data Fig. 1). Then, we removed coordinate fluctuations due to multipath[53-54]. Multipath signals are known to appear periodically, so we estimated them using STL[55-56] which decomposes time series into trend, seasonal (i.e., periodic) and residual terms. Here, we chose 86100 seconds for the period because it is the integer multiple of the sampling interval closest to the typical multipath period (86154 seconds[54]). We removed the estimated seasonal component and kept the other two terms for the subsequent analysis (red in Extended Data Fig. 1). Next, we removed diurnal variation in the data, using the same approach for the multipath removal but with a period of 86400 seconds[57] (pink in Extended Data Fig. 1). Next, we removed common mode error which originates from the fluctuation of the reference frame and satellite orbit errors[58]. We extracted common mode error by stacking time series at 6 sites in the nodal direction of the mainshock and aftershock, where little coseismic deformation is expected (Fig. 1 and orange in Extended Data Fig. 1). Before stacking them, we removed outliers and a linear trend of time series at each site. The outliers are defined as epochs satisfying the following criterion (Equation (1))[57];

$$\left| u_i - \frac{q_1+q_3}{2} \right| > n * \frac{q_3-q_1}{2} \quad (1)$$

where, u_i is the displacement at the i-th epoch, q_1 and q_3 are the 25 and 75 percentile values of the position time series, respectively, derived from data between 60 days before and 30 days after the day of mainshock. The term n is a threshold controlling how strict or loose we impose the outlier criterion and we adopted $n = 8$ in this study based on trial-and-error approaches. We estimated and removed the linear trend from the data after this outlier removal step.

Trajectory function fitting to cleaned high-rate GPS coordinates

To extract crustal deformation of the mainshock, the interevent stage, the largest aftershock and the subsequent postseismic stage (2 days), we carry out a trajectory model fit to the cleaned GPS data (blue in Extended Data Fig. 1) between 5 days before and 30 days after the day of mainshock. Our trajectory model $x(t)$ is defined as follows;

$$x(t) = a + \left\{ b + c\, log\left(1 + \frac{t-t_0}{d}\right) \right\} H(t-t_0) + \left\{ e + f\, log\left(1 + \frac{t-t_1}{g}\right) \right\} H(t-t_1) \quad (2)$$

where a is the initial position of the time series in the time window, b and e are coseismic offsets of the mainshock (at time $t = t_0$) and the largest aftershock (at $t = t_1$), respectively, $c\, log\left(1 + \frac{t-t_0}{d}\right)$ and $f\, log\left(1 + \frac{t-t_1}{g}\right)$ represent postseismic responses induced by the mainshock and the largest aftershock, respectively and the term $H(t)$ is the Heaviside's step function. We used a logarithmic function for modelling the postseismic deformation, which is considered to represent velocity-strengthening afterslip[6,31,59]. At the earlier stage of this study, we attempted to fit different functions[11,60], but fluctuations left in the data did not allow us to significantly distinguish them. We determined the time constant(s) of the logarithmic term(s) and the other parameters by grid search and the least square regression, respectively. The search range for d and g is 0.1 – 3 days and 0.1 – 10 days, respectively. For sites around the Peru and Chile border (i.e., those north of 19°S), we excluded the term relating to the largest aftershock (i.e., the third term of Equation (2)) and set the search range for d as 0.1 – 10 days by considering the largest aftershock size and the great hypocentre distance.

Coordinates at some sites contain enigmatic outliers. Hence, we applied this fitting process twice. We used Equation (2) in both steps, but, after the first fit, we removed epochs, which deviate from the model prediction by 3 times post-fit RMS, as outliers. RMS is here defined as

$$RMS = \sqrt{\frac{\sum_{i=1}^{n} \left(\frac{o(t_i)-x(t_i)}{w(t_i)}\right)^2}{\sum_{i=1}^{n} \frac{1}{w(t_i)^2}}} \quad (3)$$

where, $o(t_i)$ and $w(t_i)$ are a coordinate and its error at $t = t_i$, respectively and n is the number of available epochs. Then, we again fit the same function to the data without the outliers.

We retrieved surface deformation at the four stages from the trajectory model fit result (Figs. 1c-e and Extended Data Figs. 2a-c and 3a-f), which would be subsequently inverted for the interface slip (See next section). Amplitudes of the two step terms (i.e., b and e) are taken as coseismic displacements of the two quakes at each site (Extended Data Figs. 3a-b and 3d-e). For simplicity, the formal displacement errors are obtained by the linear least-square transformation of the GPS position observation errors. Displacements associated with the interevent afterslip and afterslip following the largest aftershock are retrieved as increments of the model prediction for each stage (Fig. 1b and Extended Data Figs. 2d, 3c and 3f). Here, we rely only on the cumulative displacement during 27 hours between the two quakes predicted from the second fit of Equation (2). We do not discuss the temporal evolution process with this trajectory model fit result because the noise left in the data and the short data duration for the interevent stage did not allow us to determine these values meaningfully (Extended Data Fig. 7), even though the input GPS coordinates for these fitting operations went through the cleaning process. For simplicity, formal errors for the displacements at these two aseismic stages were defined as Equation (3) except for the data length; we computed RMS with the data and the model prediction during each time window.

Motogram and incremental interevent displacements

As stated above, the function fit has the meaningful role only to extract cumulative displacements during the interevent stage. Yet, to take a closer look into interim details of interevent processes, we computed the moving median of the cleaned GPS coordinates with a window length of 0.5 days (Fig. 4b) after removing the estimated coseismic steps associated with the mainshock and the largest aftershock. We did not exclude the pre-mainshock or post-largest-aftershock coordinates when deriving the moving median for the first or last 0.25 days because, given the definition of median, distortion of the obtained moving median should be limited. Using the shorter window length by excluding these pre-mainshock or post-largest-aftershock coordinates from the calculation would have larger impacts.

We employed the obtained interevent moving median curve to derive the other dataset of interevent displacement field (Extended Data Figs. 8a-b) as well as their incremental displacements during the first and the last halves of the interevent window (Figs. 4e-f and Extended Data Figs. 8c-d). We took the difference of two positions among the first, the middle and the last epochs of the moving median to derive these displacements at the three windows. For simplicity, formal errors of the displacements are taken from the trajectory analysis result.

Slip inversion

We inferred slip distribution for the mainshock (Extended Data Fig. 3g), the largest aftershock (Extended Data Fig. 3h) and the interevent and post-largest-aftershock (Extended Data Fig. 3i) afterslip by performing slip inversion. For the interevent afterslip, we used four different data sets, namely, (i) the cumulative interevent displacements derived from the trajectory model fit (i.e., Equation (2); Figs. 1b and 2a and Extended Data Figs. 2d-e), (ii) same as (i) but displacements derived from the moving median (Extended Data Figs. 8a-b), (iii) displacements during the first half of the interevent window, derived from the moving median (Fig. 4e and Extended Data Fig. 8c) and (iv) same as (iii) but during the second half (Fig. 4f and Extended Data Fig. 8d).
We employ a slip inversion code SDM[61]. Surface displacement due to slip on embedded faults in the homogeneous isotropic elastic half-space is used for green's function[62]. We tessellated megathrust fault surface (Slab 2)[50] with rectangle subfaults. We constrain the rake range to be inferred between 45 and 135 degrees. Slip roughness constraint is also imposed to regularise the inversion problem and we determine its strength based on a trade-off curve of data misfit versus slip roughness (Extended Data Figs. 9-10). We checked slip models with different roughness to grasp their robust features instead of resolution tests. For the cumulative interevent afterslip, taking a smoother solution makes the afterslip peak between the mainshock and the largest aftershock epicentres less notable, but residuals at the nearest coastal sites become larger (Extended Data Figs. 9c-d). Therefore, this also highlights the necessity of the south slip peak together with the forward modelling test (Extended Data Fig 4). For all the stages, we inverted the three components of GPS displacements and they are weighted according to the formal error obtained through the trajectory model fit. We used 30 GPa for rigidity to compute seismic moment (and hence moment magnitude) and coulomb stress change.
For inversions of the interevent afterslip with the datasets derived from the moving median analysis (i.e., datasets (ii), (iii) and (iv); Figs 4e-f and Extended Data Fig. 8), we excluded GPS sites located north of 19°S, namely those near the border of Chile and Peru, because including them highly destabilised the slip inversion. They are far from the area of interest for the detailed temporal analysis and therefore less or not sensitive anyway. Furthermore, to obtain the consistent slip pattern in all the interevent slip models, we added a constraint to the upper bound of the slip amplitude. For the cumulative slip inversion with dataset (ii), the upper bound is set to those obtained by the inversion of displacements obtained by the trajectory model fit (i.e., dataset (i)). The obtained slip amplitude was subsequently used as the upper bound of slip amplitude during the first and second halves of the interevent window with the datasets (iii) and (iv).

Coulomb stress change calculation

We computed coulomb stress change (CSC)[21] associated with the mainshock and the interevent aftershock (Extended Data Fig. 5). CSC is defined as follows.

$$CSC = \Delta\tau + \mu\Delta\sigma \quad (4)$$

where, $\Delta\tau$ and $\Delta\sigma$ indicate elastic shear and normal stress change induced by slip, respectively. Positive $\Delta\tau$ is taken in a hypothetical slip direction of receiver fault defined as the convergence direction of Nazca and South American plates. Positive $\Delta\sigma$ is taken in an unclamping direction. The term μ is a static effective frictional coefficient which was set to 0.4.

Seismicity analysis

We carried out analyses of seismicity count (Fig. 4c) and moment (Fig. 4d) for two regions which are divided at 20.2°S within a range from 71.5°W to 70.0°W. We calculated the number of events within a window of 0.002 days and integrated them to get the cumulative event count over time, which were normalised by the final value before the largest aftershock. We calculated the moment of seismicity with the same window size. Here, we defined moment of seismicity for each event as $10^{1.5M_L}$ where M_L is local magnitude provided by the seismicity catalogue[34]. If local magnitude linearly scales with moment magnitude with a proportion coefficient of 1 (i.e., $M_L = M_w + const.$)[63], the time evolution of cumulative seismicity moment derived in this study exactly represents the seismic moment evolution after the normalisation. Hence, we interpret only the time evolution of the normalised seismicity count and moment.

References

51. Blewitt, G., Hammond, W. C. & Kreemer, C. Harnessing the GPS data explosion for interdisciplinary science. *Eos, **99*** (2018).
52. Altamimi, Z., Métivier, L., Rebischung, P. et al. ITRF2014 plate motion model. *Geophys. J. Int.* **209**, 1906–1912 (2017).
53. Bock, Y., Nikolaidis, R. M., de Jonge, P. J. et al. Instantaneous geodetic positioning at medium distances with the Global Positioning System. *J. Geophys. Res.* **105**, 28223–28253 (2000).
54. Ragheb, A. E., Clarke, P. J. & Edwards, S. J. GPS sidereal filtering: Coordinate- and carrier-phase-level strategies. *J. Geod.* **81**, 325–335 (2007).
55. Cleveland, R. B., Cleveland, W. S., McRae, J. E. et al. STL: A seasonal-trend decomposition procedure based on loess. *J. Off. Stat.* **6**, 3–73 (1990).
56. Pedregosa, F., Varoquaux, G., Gramfort, A. et al. Scikit-learn: Machine learning in Python. *JMLR* **12**, 2825–2830 (2011).
57. Itoh, Y., Aoki, Y. & Fukuda, J. Imaging evolution of Cascadia slow-slip event using high-rate GPS. *Sci Rep* **12**, 7179 (2022).
58. Wdowinski, S., Bock, Y., Zhang, J. et al. Southern California permanent GPS geodetic array: Spatial filtering of daily positions for estimating coseismic and postseismic displacements induced by the 1992 Landers earthquake. *J. Geophys. Res.* **102**, 18057–18070 (1997).
59. Marone, C. J., Scholtz, C. H., & Bilham, R. On the mechanics of earthquake afterslip, *J. Geophys. Res.* **96**, 8441– 8452 (1991).
60. Periollat, A., Radiguet, M., Weiss, J. et al. Transient brittle creep mechanism explains early postseismic phase of the 2011 Tohoku-Oki megathrust earthquake: Observations by high-rate GPS solutions. *J. Geophys. Res.* **127**, e2022JB024005 (2022).
61. Wang, L., Wang, R., Roth, F. et al. Afterslip and viscoelastic relaxation following the 1999 M 7.4 Izmit earthquake from GPS measurements, *Geophys. J. Int.*, **178**, 1220-1237 (2009).
62. Okada, Y. Internal deformation due to shear and tensile faults in a half-space. *Bull. Seism. Soc. Am.* **82**, 1018–1040 (1992).
63. Hanks, T. C., & Kanamori, H. A moment magnitude scale, *J. Geophys. Res.* **84**, 2348– 2350 (1979).
64. Sandwell, D. T., Müller, R. D., Smith, W. H. F. et al. New global marine gravity model from CryoSat-2 and Jason-1 reveals buried tectonic structure. *Science*, **346**, 65-67 (2014).
65. Smith, W. H. F. & Sandwell, D. T. Global seafloor topography from satellite altimetry and ship depth soundings. *Science* **277**, 1957-1962 (1997).

Data availability

We processed publicly available data and no new data was acquired for this work. The 5-minute GPS coordinates[51] are available at http://geodesy.unr.edu/. The seismicity catalogue of Soto et al.[46] is available at https://datapub.gfz-potsdam.de/download/10.5880.GFZ.4.1.2019.009/Iquique_earthquake_seismicity_catalogue_2014.tx

t. The gravity anomaly[64] and topography[65] data are available at https://topex.ucsd.edu/cgi-bin/get_data.cgi. Other previously published materials are available upon request to their authors or supplemented to their publications. We made our slip distribution of the interevent afterslip available in xxx (ready at publication).

Code availability

The inversion code SDM[61] is available at https://gfzpublic.gfz-potsdam.de/pubman/item/item_1975902.

Acknowledgements

Discussion with Jorge Jara, Zaccaria El Yousfi, Michel Bouchon, Satoshi Ide, Jean-Philippe Avouac, and Sylvain Barbot was fruitful. Nadaya Cubas provided us with her research product of Cubas et al.[38] English check by James Hollingsworth was helpful in improving the manuscript. Y.I. is a Japan Society for the Promotion of Science (JSPS) Overseas Research Fellow. This work has been supported by ERC CoG 865963 DEEP-trigger (A.S.).

Author contributions

All the authors designed the study, interpreted and discussed the results and reviewed and edited the manuscript. Y.I. carried out all the analyses, made the figures and wrote the original manuscript. Y.I. and A.S. acquired the grants.

Competing interests

The authors declare no competing interests.

Extended Data

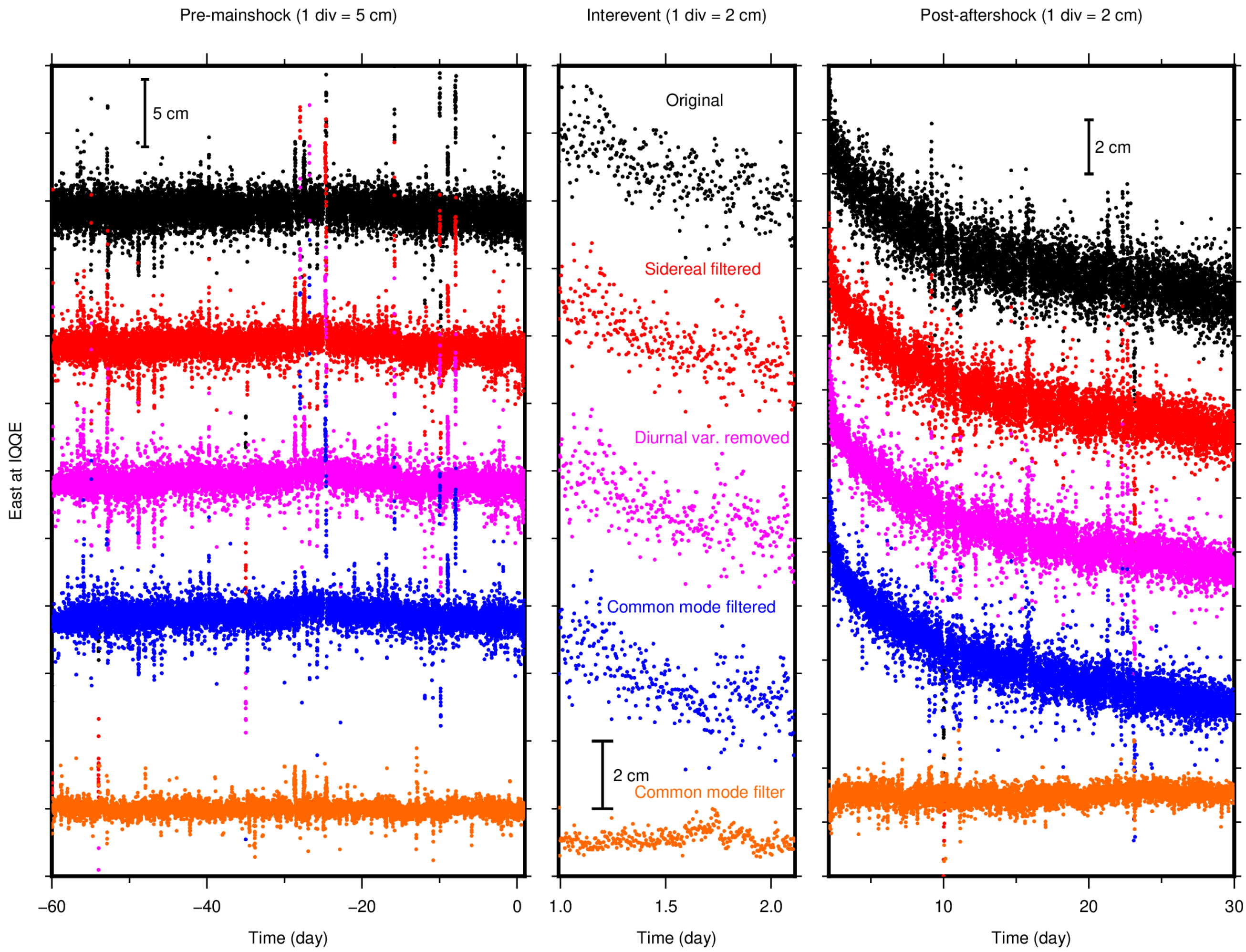

Extended Data Figure 1. High-rate 5-min GPS data cleaning procedure (East component at IQQE as an example; Fig 1b). Time series with each colour indicate results of cleaning procedure at each step as labelled (See Methods). Coseismic steps of the mainshock and the largest aftershock are removed by breaking panels.

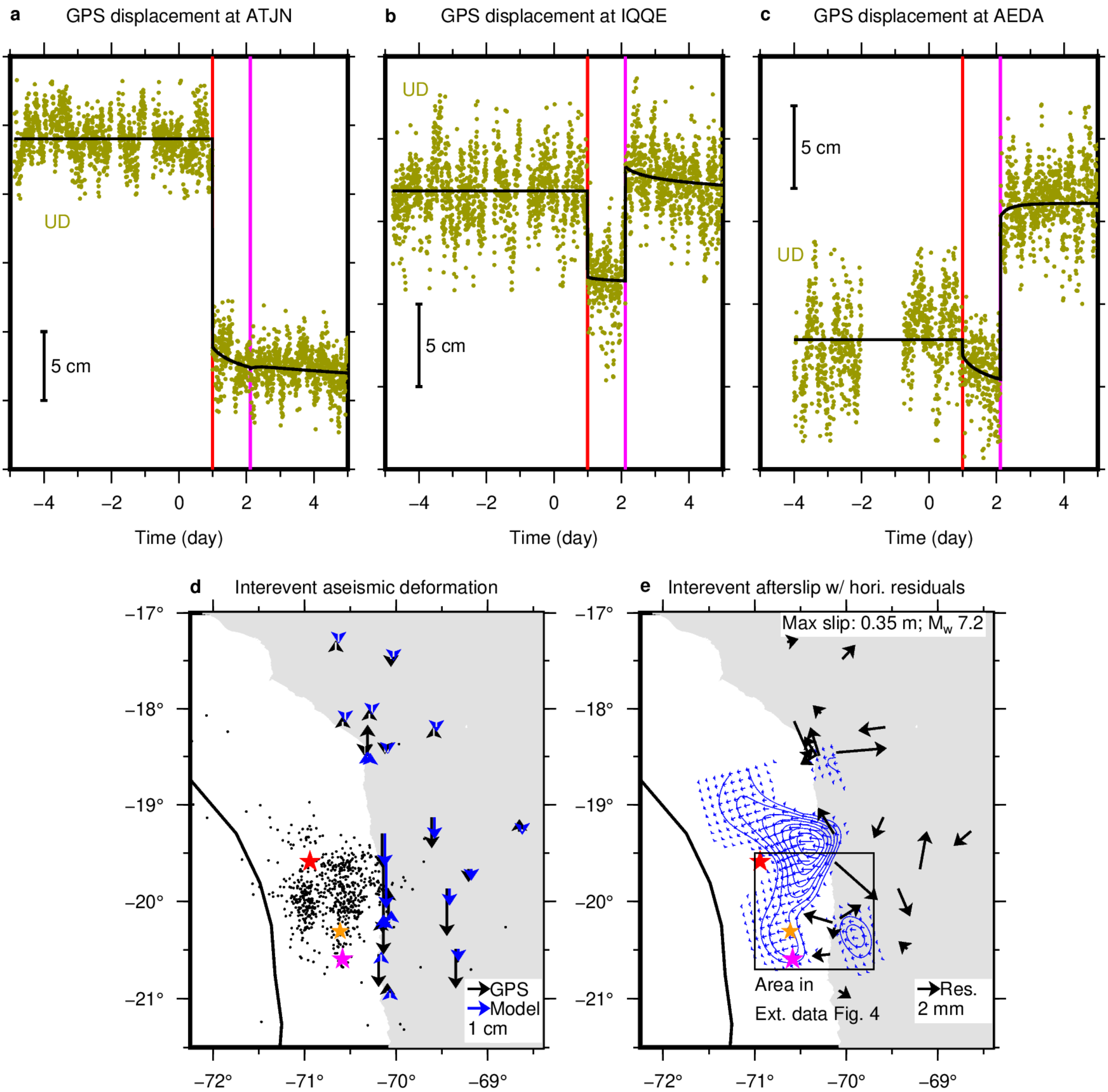

Extended Data Figure 2. Data analysis and slip inversion result using the trajectory function fit approach. **a**-**c**, Trajectory model fit results for vertical components at three sites as labelled. Location of these sites is shown in Fig. 1**b**. **d**, Vertical GPS displacements (black vectors) during 27 hours between the mainshock and the largest aftershock, together with model prediction (blue vectors) from aseismic slip inversion shown in **e** and Fig. 2a. Refer to Fig. 2 for other elements. **e**, The inferred interevent afterslip (blue contours) with normalised slip vectors. Black vectors indicate horizontal residuals of the inversion (GPS – Model in Fig. 1b).

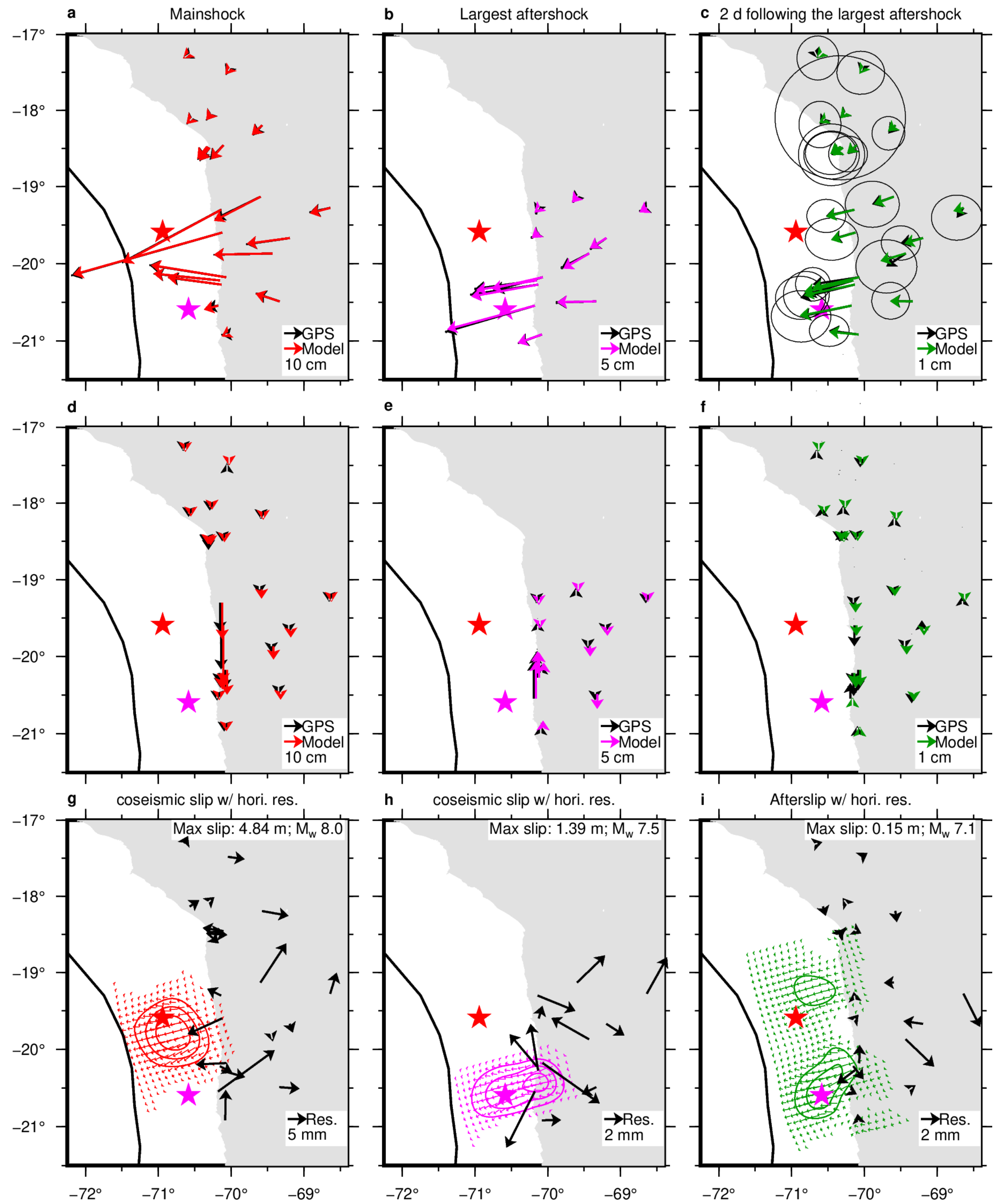

Extended Data Figure 3. Data analysis and inversion results for the mainshock (**a**, **d** and **g**), the largest aftershock (**b**, **e** and **h**) and the post-largest-aftershock stage (2 days; **c**, **f** and **i**). **a**-**c**, Horizontal GPS displacements at each stage derived from the trajectory model fit. **d**-**f**, Same as **a**-**c** but for vertical displacements. **g**-**i**, Slip inversion results (contours) at each stage with normalised slip vectors. Black vectors indicate horizontal residuals of the inversion (GPS – Model).

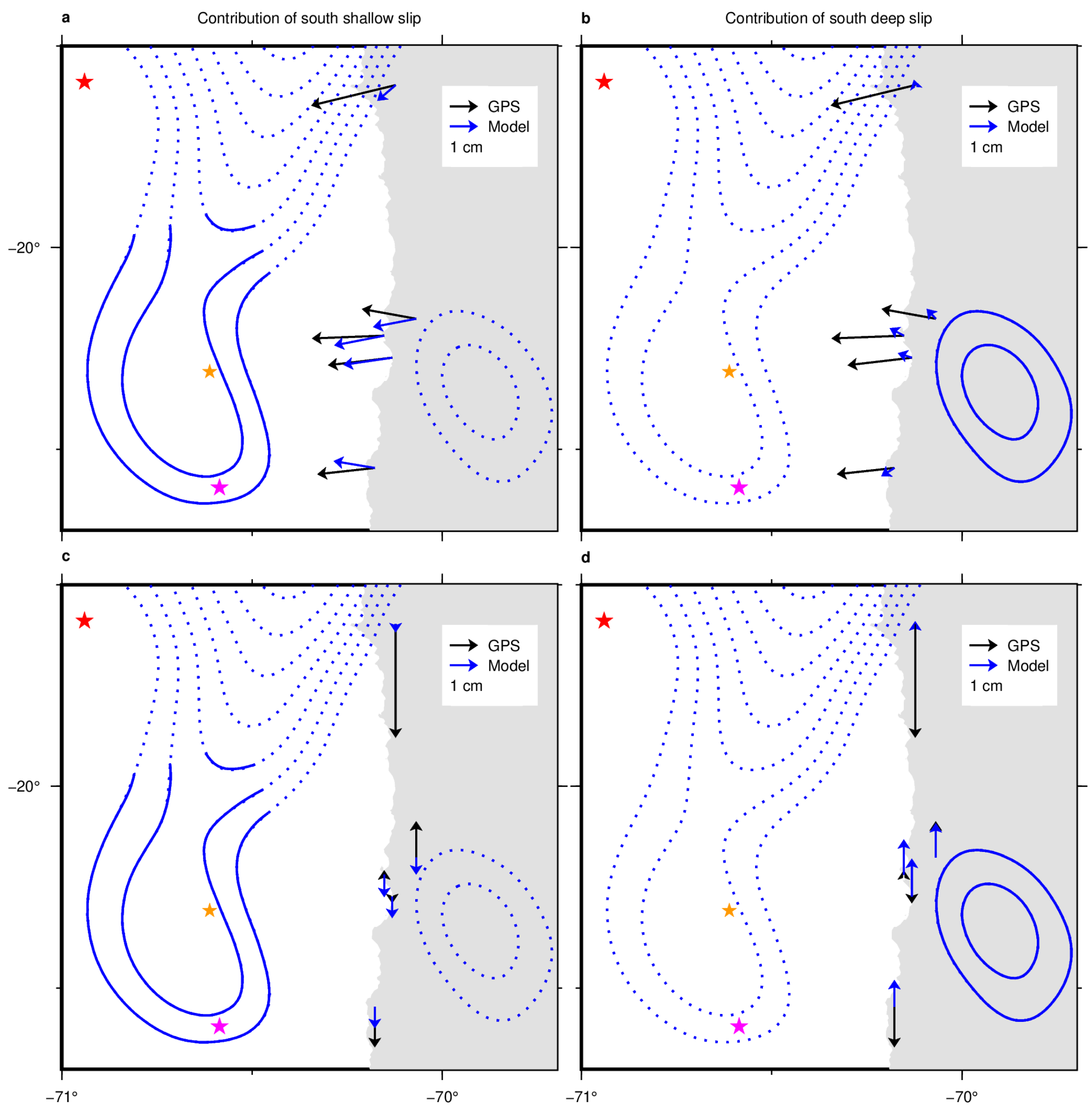

Extended Data Figure 4. Forward modelling test results for the interevent afterslip. Comparison of interevent GPS displacements derived from the trajectory model fit (black) and model prediction (blue) computed from subset (solid contours) of interevent afterslip inferred from the black vectors (solid + dot contours). **a-b**, Comparison of horizontal displacements. **c-d**, Same as **a-b** but for vertical displacements. Refer to Extended Data Fig. 2e to identify the plot area.

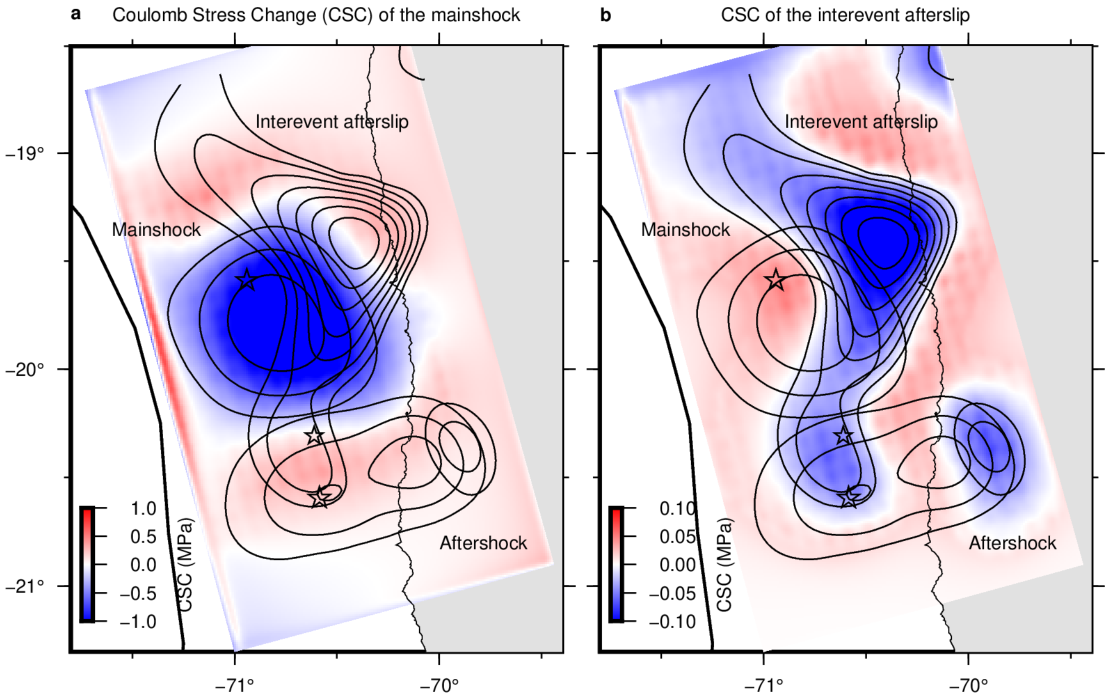

599
600 **Extended Data Figure 5.** Coulomb stress change (CSC) associated with the mainshock (**a**) and the
601 interevent afterslip (**b**). Solid contours are slip distribution of the mainshock, the interevent afterslip
602 and the largest aftershock, as labelled. Refer to Fig. 2 for contour interval and open stars.
603

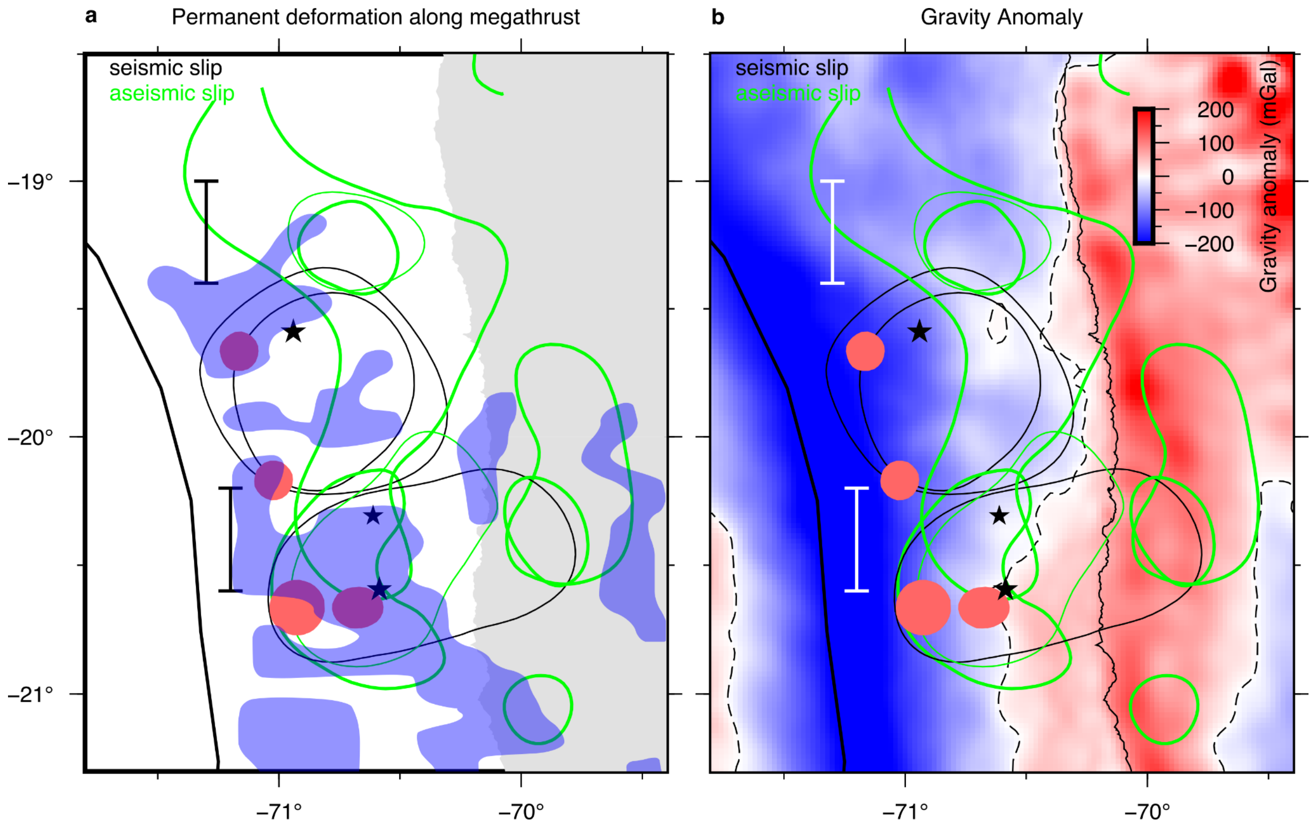

Extended Data Figure 6. a. Slip events at different stages with outline of areas possibly hosting multiple faults subparallel to the megathrust[38] (blue shapes). Seismic and aseismic slip events at different stages (Fig. 3a) are drawn with black and green contours, respectively, for clarity. **b.** Same as **a** but with gravity anomaly[64] (background colour) with zero value outlined with broken contours. Refer to Fig. 1a for other elements.

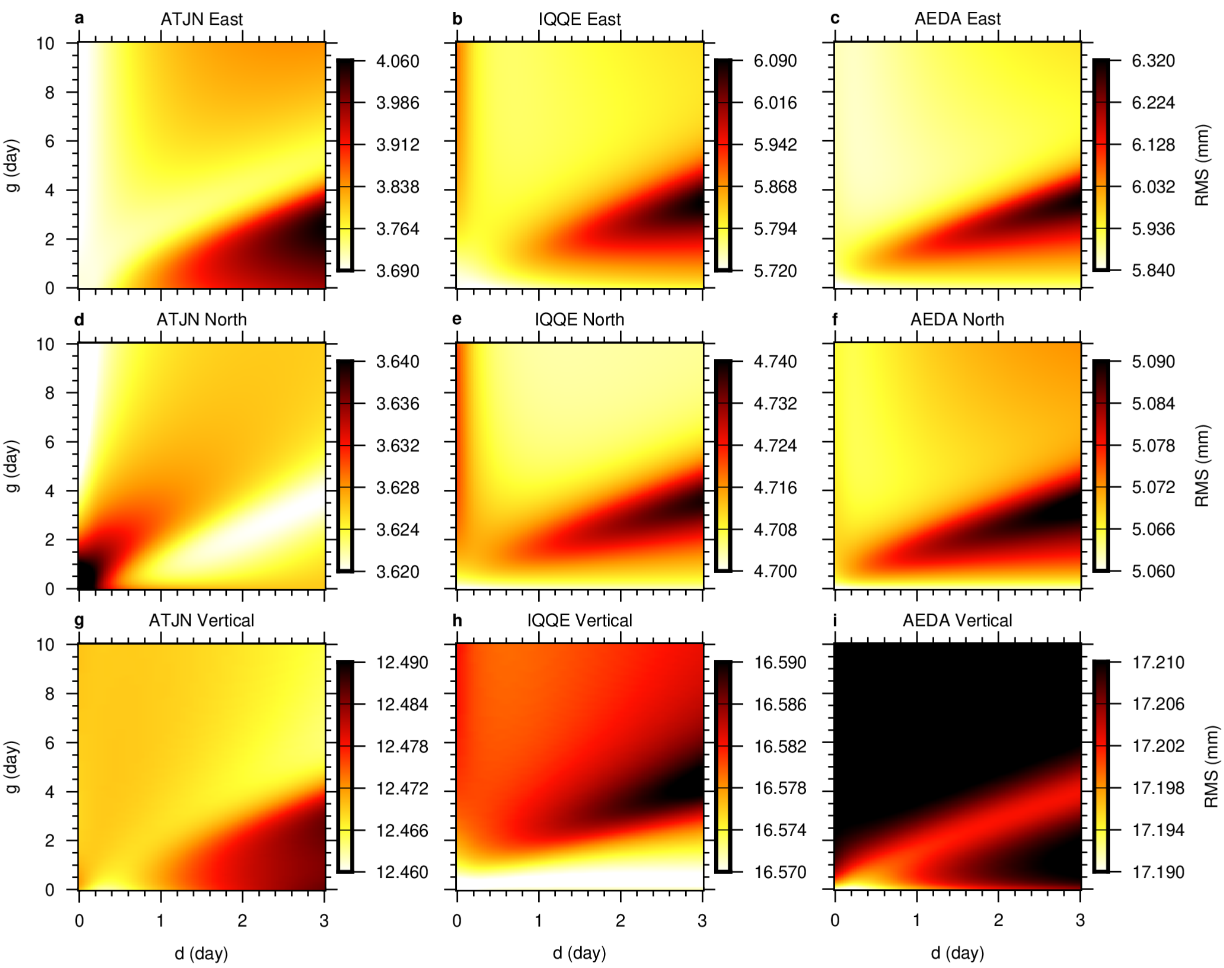

Extended Data Figure 7. Distribution of RMS of the trajectory model fit with respect to different *d* and *g* in Equation (2) (colour). **a-c**, Results for the east component at three sites as labelled. Site location is shown in Fig. 1b. **d-f** and **g-i**, Same as **a-c** but for the north and the vertical components, respectively.

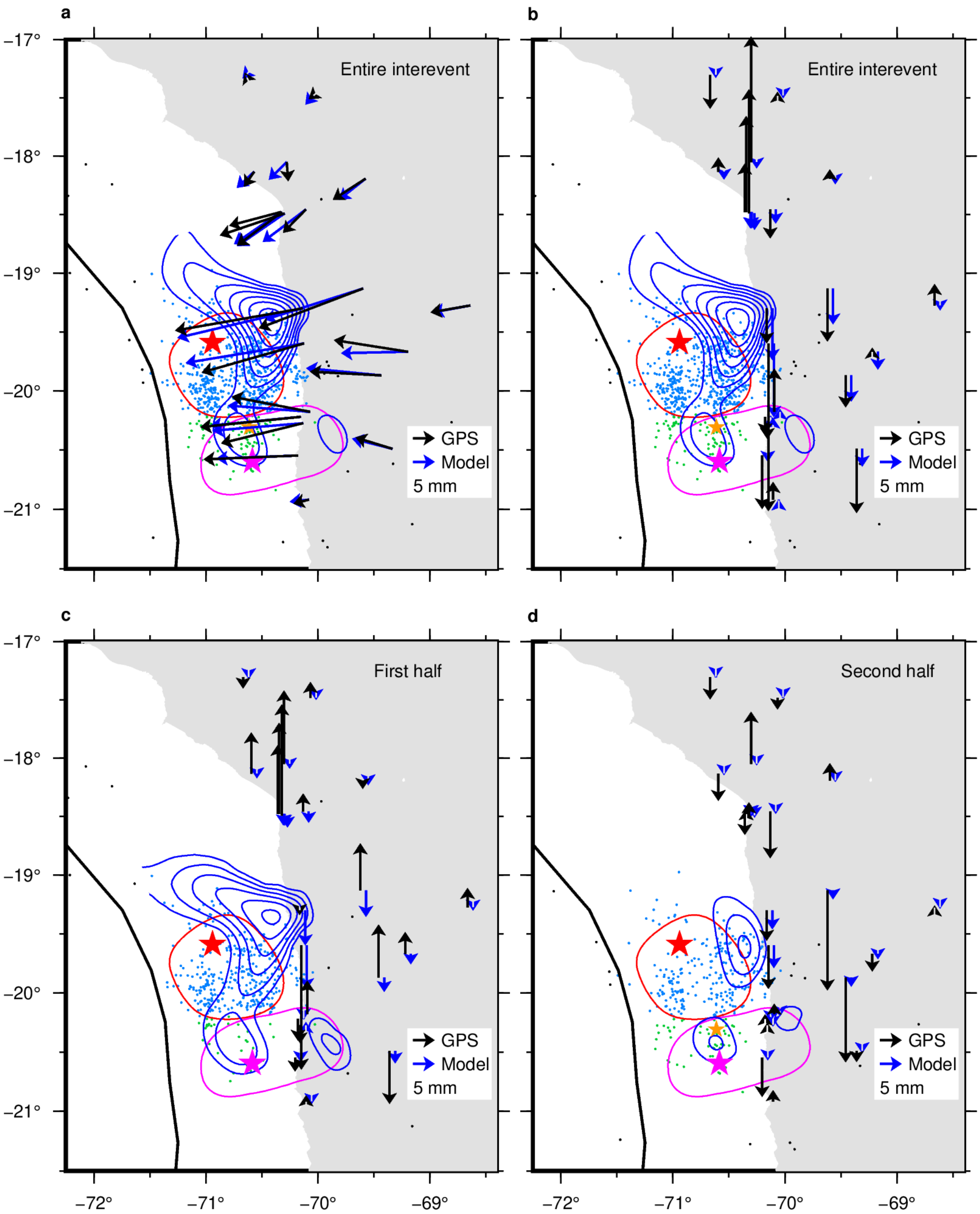

Extended Data Figure 8. Data analysis and slip inversion result using the moving average approach. **a-b**, Cumulative interevent horizontal (**a**) and vertical (**b**) displacements (black vectors) derived from the moving average analysis, together with the model prediction (blue vectors) from the inferred afterslip (blue contours). Refer to Fig. 4 for other elements. Note that GPS displacements at sites north of 19°S are not inverted. **c-d**, Same as Figs. 4e-f but with vertical GPS displacements derived from the moving average analysis (black vectors) and model predictions (blue vectors)

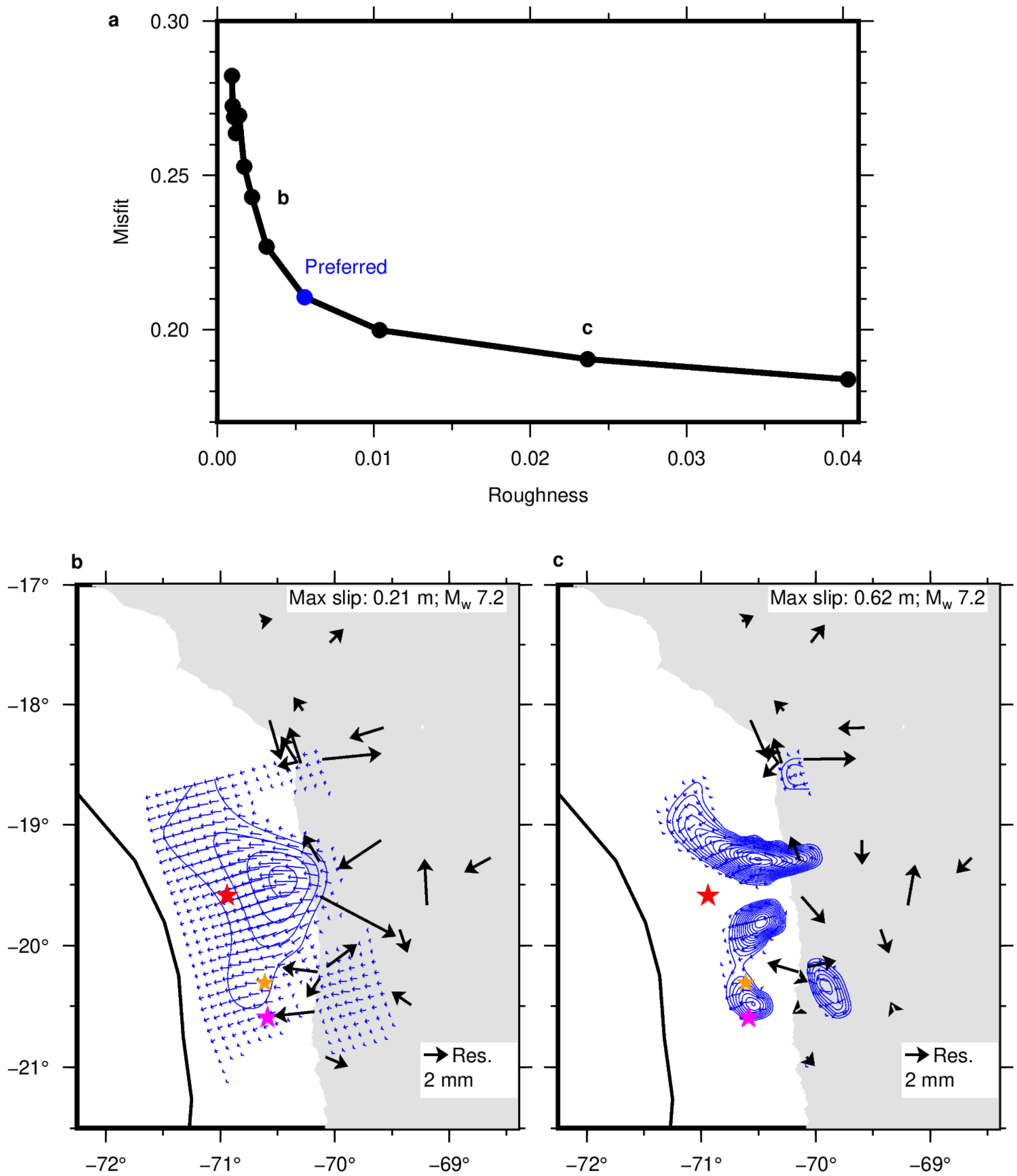

Extended Data Figure 9. Trade-off curve of the slip roughness and misfit and model variations for the interevent afterslip inversion using the displacements derived from the trajectory model fit. **a**, Trade-off curve. Dots indicate preferred (blue) and other tested models. **b**-**c**, model variation with different slip roughness as shown in **a**. Refer to Extended Data Fig. 2e for other elements.

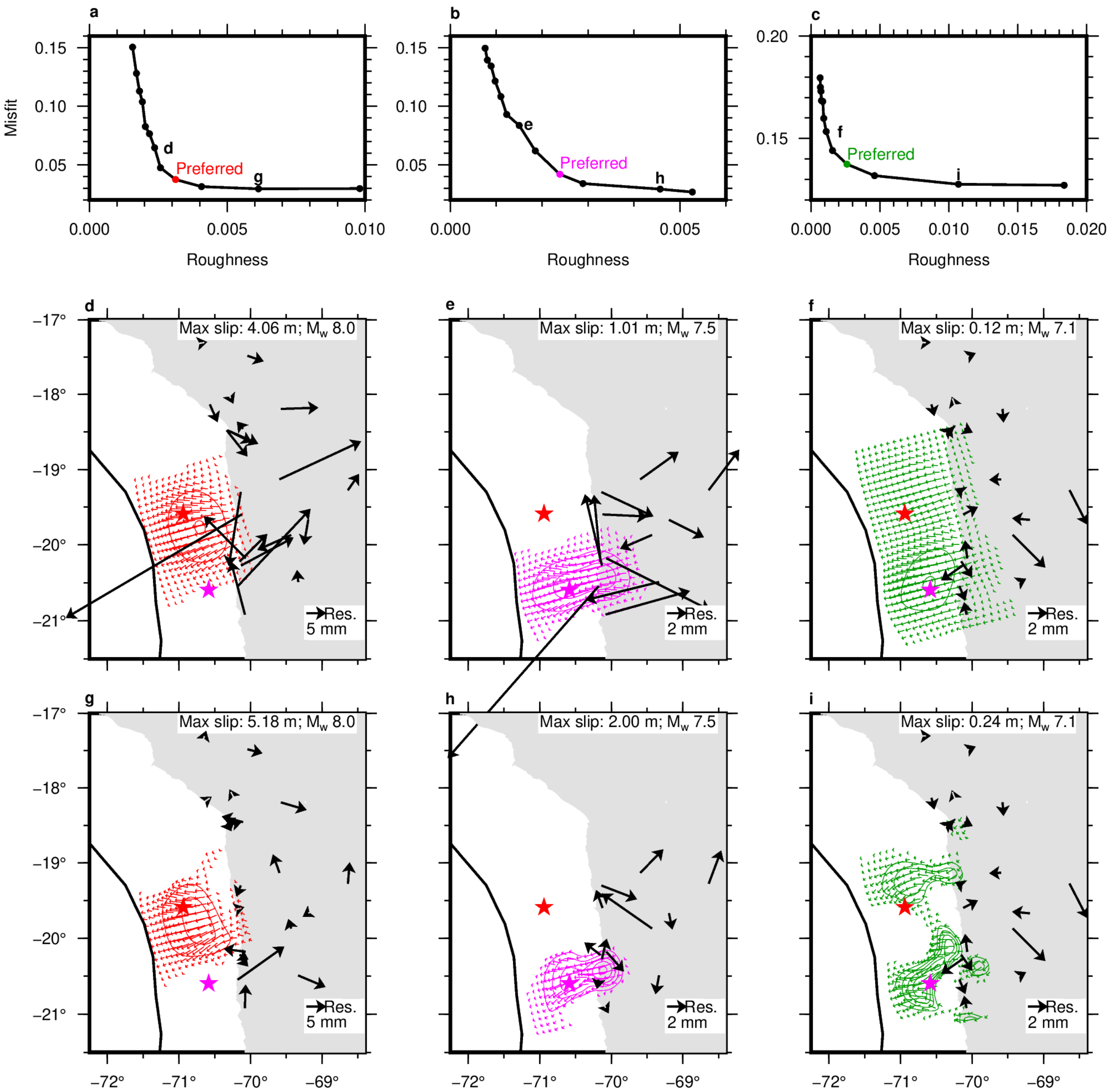

Extended Data Figure 10. Trade-off curve of the slip roughness and misfit and model variations for the mainshock, the largest aftershock and subsequent 2-day afterslip. **a**-**c**, Trade-off curve for the mainshock (**a**), the largest aftershock (**b**) and subsequent 2-day afterslip (**c**). Dots indicate preferred (red, purple or green) and other tested models. **d**-**i**, model variation with different slip roughness as shown in **a**-**c**. Refer to Extended Data Figs. 3**g**-**i** for other elements.